nature photonics

ARTICLES

https://doi.org/10.1038/s41566-022-01024-9

Check for updates

OPEN

Synergistic strain engineering of perovskite single crystals for highly stable and sensitive X-ray detectors with low-bias imaging and monitoring

Jizhong Jiang[1,6], Min Xiong[2,6], Ke Fan[3], Chunxiong Bao[4], Deyu Xin[5], Zhengwei Pan[2], Linfeng Fei[2], Haitao Huang[3], Lang Zhou[2], Kai Yao[2]✉, Xiaojia Zheng[5], Liang Shen[1]✉ and Feng Gao[4]✉

Although three-dimensional metal halide perovskite (ABX_3) single crystals are promising next-generation materials for radiation detection, state-of-the-art perovskite X-ray detectors include methylammonium as A-site cations, limiting the operational stability. Previous efforts to improve the stability using formamidinium–caesium-alloyed A-site cations usually sacrifice the detection performance because of high trap densities. Here we successfully solve this trade-off between stability and detection performance by synergistic composition engineering, where we include A-site alloys to decrease the trap density and B-site dopants to release the microstrain induced by A-site alloying. As such, we develop high-performance perovskite X-ray detectors with excellent stability. Our X-ray detectors exhibit high sensitivity of $(2.6 \pm 0.1) \times 10^4\ \mu C\ Gy_{air}^{-1}\ cm^{-2}$ under $1\ V\ cm^{-1}$ and ultralow limit of detection of $7.09\ nGy_{air}\ s^{-1}$. In addition, they feature long-term operational stability over half a year and impressive thermal stability up to 125 °C. We further demonstrate the promise of our perovskite X-ray detectors for low-bias portable applications with high-quality X-ray imaging and monitoring prototypes.

Three-dimensional metal halide perovskites with the general formula of ABX_3 have shown great success in different optoelectronic devices, including solar cells, light-emitting diodes (LEDs) and detectors[1–4]. For radiation detection, metal halide perovskites with attractive properties (for example, large X-ray attenuation coefficient (α), great mobility–lifetime product and unique defect-tolerant nature) have been considered as promising candidates for X-ray detectors with high sensitivity, high signal-to-noise ratio (SNR) and low limit of detection (LoD)[5–8]. However, methylammonium (MA) remains the dominant A-site cation in perovskite single crystals used for high-performance X-ray detectors, with $MAPbI_3$ being the most commonly used[9–14]. These volatile MA cations cause stability issues, limiting the long-term reliability of perovskite X-ray detectors[14–16].

To improve the stability, it is attractive to shift from MA to caesium (Cs) and formamidinium (FA), often in the form of Cs–FA alloys for optimal tolerance factor and structural stability[17–19]. A successful example is the mixed-cation/halide $Cs_xFA_{1-x}Pb(I_{1-y}Br_y)_3$ with much enhanced stability[17,20]. Despite these advances, mixed cations and halides bring new challenges in the kinetic control of homogeneous crystal growth. As a result, the performance of these mixed Cs–FA perovskite detectors usually show inferior performance due to the presence of crystal imperfections[21,22], including dislocations and vacancies[23,24]. For instance, halide vacancies dominate in mixed-cation perovskites due to their low formation energy[25–27]. In addition, there are several attempts to incorporate B-site dopants for improving the optoelectronic properties of these mixed-cation/halide perovskites[28–31]. However, the influences of B-site doping have been inconsistent. For example, some reports show that impurity metal ions would disrupt the crystal symmetry and increase the electronic disorder[32–36]. Therefore, it remains challenging to rationally design A-site alloying and B-site doping for perovskite crystals with superior performance and excellent stability simultaneously.

Here we address these challenges and develop high-performance perovskite X-ray detectors with excellent stability. We make use of the strong bonding between guanidinium (GA) and iodide, and decrease the halide vacancies by incorporating GA into stable Cs–FA iodide-based perovskites. The detrimental tensile strain caused by oversized GA incorporation leads to unfavourable relaxation via Pb vacancies and hence inhomogeneous stress. We then introduce a low concentration of strontium (Sr) to the B site to increase the energetic cost associated with the formation of Pb vacancies, prohibiting this unfavourable channel for strain relaxation. With synergistic strain engineering on both A and B sites, our stable MA-free perovskite single crystals show excellent optoelectronic properties, enabling a high-performance X-ray detector with ultralow LoD of $7.09\ nGy_{air}\ s^{-1}$ and high sensitivity of $(2.6 \pm 0.1) \times 10^4\ \mu C\ Gy_{air}^{-1}\ cm^{-2}$ at $1\ V\ cm^{-1}$ and $(2.5 \pm 0.2) \times 10^6\ \mu C\ Gy_{air}^{-1}\ cm^{-2}$ at $400\ V\ cm^{-1}$.

Results and discussions

A-site alloying of MA-free perovskites. We start with the structurally stable $Cs_{0.1}FA_{0.9}Pb(I_{0.9}Br_{0.1})_3$ (denoted as CsFA) single crystals (Fig. 1a)[17,20,37], grown using a modified inverse temperature crystallization method (Supplementary Fig. 1)[20,38]. As shown in Supplementary Fig. 2, the X-ray diffraction (XRD) pattern of our CsFA single crystals shows no signs of impurities. Compared with

[1]State Key Laboratory of Integrated Optoelectronics, College of Electronic Science and Engineering, International Center of Future Science, Jilin University, Changchun, People's Republic of China. [2]Institute of Photovoltaics, School of Physics and Materials Science, Nanchang University, Nanchang, People's Republic of China. [3]Department of Applied Physics, The Hong Kong Polytechnic University, Hung Hom, Kowloon, People's Republic of China. [4]Department of Physics, Chemistry and Biology (IFM), Linköping University, Linköping, Sweden. [5]Sichuan Research Center of New Materials, Institute of Chemical Materials, China Academy of Engineering Physics, Chengdu, People's Republic of China. [6]These authors contributed equally: Jizhong Jiang, Min Xiong. ✉e-mail: yaokai@ncu.edu.cn; shenliang@jlu.edu.cn; feng.gao@liu.se

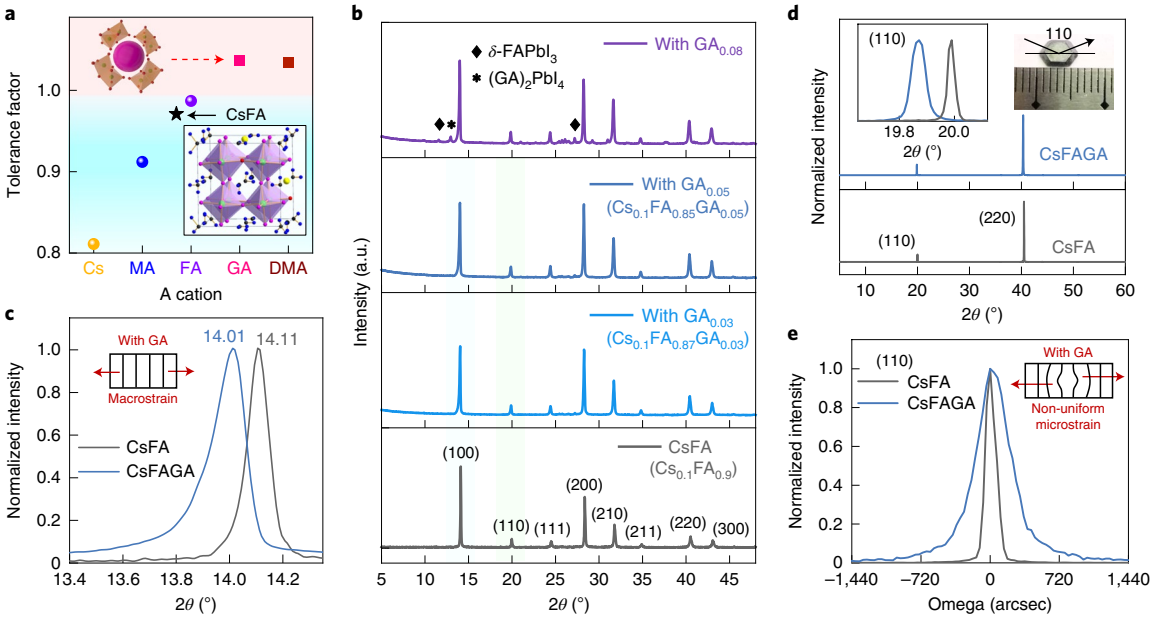

Fig. 1 | Characterizations of CsFAGA single crystals. a, Goldschmidt tolerance factor of $APbI_3$ perovskites with different A-site cations. The bottom-right inset shows the crystal structure of CsFA. The Pb atoms are depicted with green balls; Br, red; I, pink; Cs, yellow; C, black; N, blue. The top-left inset shows the structural model for $APbI_3$ with a large organic cation, such as dimethylammonium (DMA) and GA, where a 3D perovskite structure cannot be maintained. **b**, XRD patterns of grounded powders obtained from $Cs_{0.1}FA_{0.9-z}GA_zPb(I_{0.9}Br_{0.1})_3$ ($z = 0$, 0.03, 0.05, 0.08) precursor solution; for convenience, they are simplified as pristine (CsFA) and GA_z ($z = 0.03$, 0.05, 0.08) crystals, respectively. **c**, Enlarged powder XRD spectra of the (100) plane of CsFA and CsFAGA (referring to $Cs_{0.1}FA_{0.85}GA_{0.05}Pb(I_{0.9}Br_{0.1})_3$). **d**, X-ray 2$\theta$ scan on the top facet of CsFA and CsFAGA single crystals and a photograph (inset) of the CsFAGA single crystal. **e**, High-resolution XRD rocking curve of the (110) diffraction of CsFA and CsFAGA crystals. The insets in **c** and **e** show the schematic of the macrostrain and microstrain after GA incorporation, respectively.

pure $FAPbI_3$ crystals, an expected systematic shift to higher angles is observed due to the partial replacement of FA and I ions with smaller Cs and Br ions, respectively. In addition to excellent environmental stability (Supplementary Fig. 3), the CsFA crystal shows satisfying thermal stability without decomposition until 320 °C, much higher than that of $MAPbI_3$ (240 °C) (Supplementary Fig. 4).

We then demonstrate that the incorporation of a small amount of GA maintains the three-dimensional (3D) structure with cubic symmetry. As shown in Fig. 1b, the CsFA structure can accommodate the lattice tensile strain and maintain a stable perovskite structure on the alloying of a small amount of GA (from 0% to 5%). Further increasing the GA ratio (for example, 8%) results in phase separation[39–41]. These results indicate that the solubility limit of GA cations in the CsFA perovskite lattice for sustaining a stable 3D structure is around 5%. From nuclear magnetic resonance (NMR) spectroscopy and X-ray photoelectron spectroscopy (XPS) results (Supplementary Figs. 5 and 6 and Supplementary Table 1), the composition ratios (Cs/FA and I/Br) in the crystals are close to those in the feed solution. Tensile strain from the large-sized GA ions leads to the expansion of the lattice (Supplementary Fig. 7) and causes a shift in the perovskite XRD peaks towards a lower angle[41] (see the exemplified (100) reflection of Fig. 1c). We perform single-crystal XRD measurements on CsFA and $Cs_{0.1}FA_{0.85}GA_{0.05}Pb(I_{0.9}Br_{0.1})_3$ (referred to as CsFAGA), both of which show an octahedral framework in cubic symmetry (Fig. 1a, inset). The calculated lattice parameters derived from the single-crystal XRD measurements also support the lattice change (Supplementary Table 2).

Photoluminescence lifetime measurements of CsFAGA single crystals reveal a remarkably longer carrier lifetime, two times greater than that of a CsFA single crystal (Supplementary Fig. 8), indicating substantially reduced trap states in CsFAGA. In addition, the trap density of states extracted from the thermal admittance spectroscopy measurement is almost one order of magnitude lower in the CsFAGA crystal than in the pristine CsFA sample.

Microstrain in CsFAGA perovskites. Although mixed cations of Cs, FA and GA demonstrate a positive effect on suppressing non-radiative recombination, the consequent tensile strain induced by large-sized GA easily leads to non-uniform stress. Compared with CsFA, the CsFAGA crystal exhibits broadened XRD peaks (Fig. 1c), indicative of a strong microstrain (inhomogeneous strain)[35]. As shown in Fig. 1d, the incorporation of GA into the CsFA single crystal causes the shift and broadening of the peaks in the XRD pattern. We further measure the high-resolution X-ray rocking curves of the (110) and (220) peaks of the reference CsFA sample (Fig. 1e and Supplementary Fig. 9), which shows a small full-width at half-maximum (FWHM) of only 92 and 90 arcsec, respectively. In contrast, the CsFAGA samples show inferior quality with the FWHM as wide as 425 and 398 arcsec for (110) and (220), respectively. The large FWHM confirms that GA alloying introduces microstrain into the CsFAGA crystal.

Although the PbI_6 octahedra containing large GA are under more tensile strain than those in metastable $FAPbI_3$ (Fig. 1a)[42], the presence of small A-site cations (Cs^+) and X^- anions (Br^-) in the octahedron with a decreased void size of the unit cell can compensate for this tensile strain with compressive strain. Therefore, the presence of Cs and Br ions in the CsFAGA structure is critical for balancing the tolerance factor and stabilizing the cubic phase. Nevertheless, this compensation is highly dependent on the local distribution of GA in the A site. We consider different configurations of GA distribution (Supplementary Fig. 10 and Table 3), and calculate the change in enthalpy (ΔH) and defect formation energies (DFEs) using density functional theory (DFT) (Supplementary Information provides the computational details).

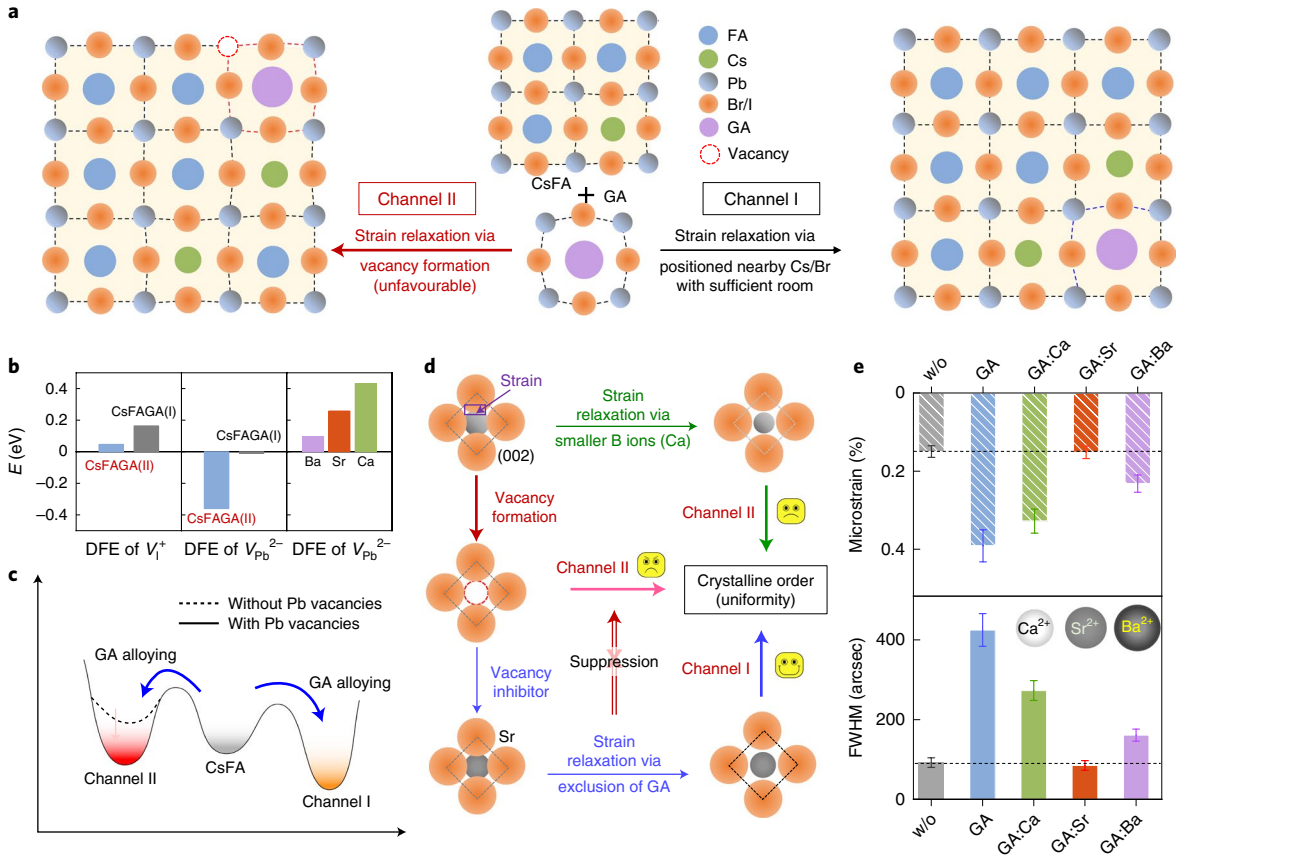

Fig. 2 | Mechanisms of microstrain reduction through B-site doping. a, Schematic of the local tensile strain in CsFAGA crystal, which can be relaxed either by compensation with compressive strain (Channel I) or by forming point defects (Channel II). **b**, DFEs of iodine vacancies (V_I^+) (left) and Pb vacancies (V_{Pb}^{2-}) (middle) of CsFAGA with respect to that of CsFA. Both supercell models of relevant CsFAGA perovskites are investigated. The right image exhibits the energy increase in Pb (V_{Pb}^{2-}) vacancy formation when Pb^{2+} are substituted with Ca^{2+}, Sr^{2+} and Ba^{2+}. **c**, Ab initio energy diagram revealing the alloying channels of the GA cation with and without Pb vacancies. Note that the relative saddle point depth is undefined. **d**, Schematic of vacancy inhibitor played by the Sr dopant in CsFAGA. The incorporation of Sr restores the local strain, which prohibits the unfavoured pathway for GA alloying and improves the structural coherence. **e**, Correlation between FWHMs from X-ray rocking curves of the (110) diffraction and microstrain from XRD line broadening of CsFA and CsFAGA crystals doped without and with alkaline-earth metal ions (0.5 mol%, feed ratio), namely, Ca^{2+}, Sr^{2+} and Ba^{2+} series; for convenience, it is simplified as w/o, GA, GA:Ca, GA:Sr and GA:Ba crystals, respectively. The error bars are from experimental and fitting uncertainties.

The most favourable GA configuration with the lowest total energy is the situation where two Cs atoms occupy the neighbouring sites of GA (Supplementary Fig. 10a). In this case, the tensile strain can be relaxed by an atomic arrangement through Channel I (Fig. 2a, right), where the reduced $R_{Pb\text{-}Br}$ of a unit cell pulls the small Cs ion away from its A site, leaving sufficient room for the nearby GA cation. Meanwhile, the calculated DFE of iodine vacancies (V_I^+) for CsFAGA shows a substantial increase by 0.16 eV compared with pristine CsFA (Fig. 2b and Supplementary Fig. 11). This is consistent with the previous report that the strong hydrogen bonds between GA and halide ions suppress halide vacancy formation[40].

Another possible yet unfavourable GA configuration is the situation where GA is next to only one Cs atom, where ΔH turns slightly positive, indicating the increased difficulty of GA introduction compared with the previous configuration. In this case, the internal tensile strain could be relieved via vacancy formation[43,44]. We account for this strain relaxation mechanism through the Channel II pathway (Fig. 2a, left, and Supplementary Fig. 12)[25,36]. Similar to Channel I, the formation of iodine vacancies in Channel II remains unlikely, given their increased formation energy compared with pristine CsFA (Fig. 2b). In contrast, compared with Channel I, we notice a remarkable decrease in Pb-vacancy formation energy by 0.36 eV. As shown in Fig. 2c, the presence of Pb vacancies significantly enhances the probability of Channel II by decreasing the formation energy of CsFAGA relative to CsFA (Supplementary Table 3), making the Pb vacancy formation a thermodynamically preferred process to stabilize the cubic phase. This unfavourable GA incorporation pathway leads to structural incoherence with different atomic arrangements and electronic disorder in the CsFAGA crystal, which explains why the incorporation of GA increases the microstrain.

Suppression of Pb vacancies via B-site dopants. To suppress this unfavourable GA configuration, we need to increase the formation energy of Pb vacancies without introducing new trap states. Based on our DFT results (Supplementary Fig. 13), we choose isovalent B-site dopants, namely, alkaline-earth metal ions (Ca, Sr and Ba), as candidates. We find that the passivation reaction of V_{Pb}^{2-} is favoured by 0.22, 0.34 and 0.38 eV for Ca^{2+}, Sr^{2+} and Ba^{2+}, respectively (Supplementary Table 4). Considering the similar ionic radius of Sr^{2+} (118 pm) and Pb^{2+} (119 pm)[45], the incorporation of Sr is chosen as a promising dopant (Supplementary Fig. 12). Interestingly, we find that the inclusion of Sr into the perovskite lattice increases the Pb-vacancy formation energy by 0.26 eV (Fig. 2b), corresponding to decreased vacancy densities by an estimated factor of 10^4. The suppression of vacancy formation is against the strain relaxation,

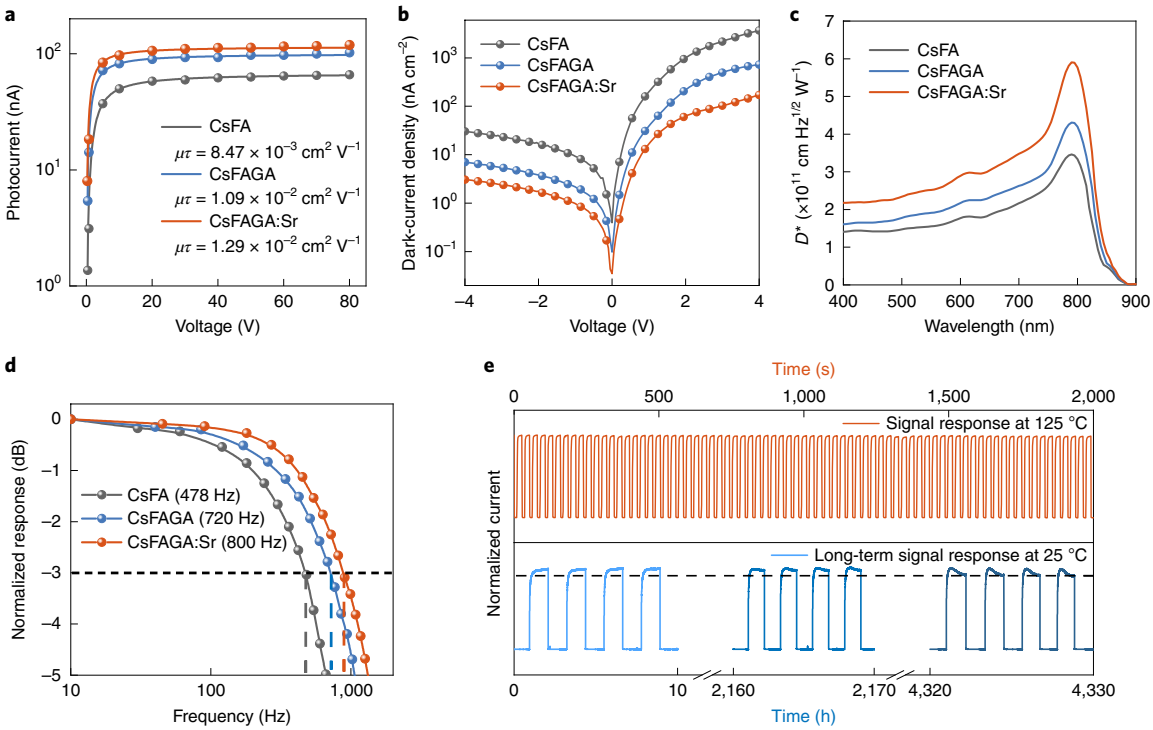

Fig. 3 | Photodetection performance of perovskite single-crystal detectors. a, Photoconductivity of CsFA, CsFAGA and CsFAGA:Sr devices. Fitting lines for the $\mu\tau$ product are also shown. **b**, Dark-current–voltage curves of the Au/perovskite/GA photodetectors. **c**, Specific detectivity spectrum of the detectors. **d**, Normalized response varying with the frequency of input signals indicates a 3 dB cutoff frequency. **e**, Long-term operational and thermal stability test on an unencapsulated CsFAGA:Sr detector. All the tests were carried out at 1 V cm^{-1}.

indicating that the incorporation of GA through Channel II is now thermodynamically unfavoured (Fig. 2d). This suggests that Sr doping in the low-doping regime is beneficial for the structural coherence of CsFAGA crystals.

Since the vacancy concentrations in halide perovskites are expected to be below 1% of Pb^{2+} ions[46,47], we prepare the CsFAGA single crystals doped with Ca^{2+}, Sr^{2+} and Ba^{2+} at sub-percent molar (0.1–1.0 mol%). We employ inductively coupled plasma optical emission spectrometry and hard X-ray photoelectron spectroscopy to quantify the exact dopant content in the crystals (Supplementary Fig. 14). At a low-doping regime (0.5 mol%, feed ratio), similar results derived from hard X-ray photoelectron spectroscopy and inductively coupled plasma optical emission spectrometry demonstrate the successful incorporation of alkaline metals into CsFAGA perovskite lattice with a uniform distribution. In addition, we find that the main compositions of the CsFAGA single crystal basically remain unchanged after doping (Supplementary Table 1). Both single-crystal and powder XRD patterns of doped CsFAGA crystals reveal no systematic shifts of the diffraction peaks (Supplementary Figs. 15 and 16), indicating the absence of macrostrain in the crystal structure under regimes with low B-site doping.

The microstrain, estimated from peak broadening, shows a notable decrease on B-site doping (Fig. 2e) and a higher dependence on metal dopants (Supplementary Figs. 17 and 18). In particular, after Sr doping, the microstrain induced by GA incorporation in the CsFAGA crystal (0.39%) decreases to a value of 0.15%, back to the level of the pristine CsFA crystal (0.15%). Furthermore, the FWHM is as low as 85 arcsec in the rocking curves of the (110) plane of Sr-doped CsFAGA (CsFAGA:Sr) single crystals (Fig. 2e and Supplementary Fig. 16), indicating enhanced structural uniformity in the crystal planes. The high-resolution transmission electron microscopy image of the CsFAGA:Sr crystal shows high-quality crystals without twinning and dislocation, with the selected area electron diffraction pattern exhibiting a homogeneous and pure cubic phase (Supplementary Fig. 19). The relative change in crystalline properties after doping is in agreement with the calculation prediction. Therefore, we conclude that the Sr dopant can be incorporated into the CsFAGA perovskite lattice as a vacancy inhibitor, which effectively prohibits lattice strain relaxation through Channel II.

Optoelectronic properties and X-ray detection performance. Encouraged by the excellent crystal properties, we move forward to investigate the properties and X-ray detection performance of our perovskite single crystals. The carrier lifetime τ composed of fast and slow decay can be obtained through time-resolved photoluminescence measurements (Supplementary Fig. 20a). The CsFAGA:Sr crystal shows longer lifetime (τ_{fast} = 94 ns; τ_{slow} = 1,059 ns), compared with that of CsFAGA (τ_{fast} = 33 ns; τ_{slow} = 523 ns). In addition, the thermal admittance spectroscopy results demonstrate a much lower density in the entire trap depth region for the CsFAGA:Sr crystal compared with the CsFAGA crystal (Supplementary Fig. 20b). All these findings are consistent with the high crystalline quality of the Sr-doped CsFAGA crystal, which minimizes unfavourable non-radiative recombination, thereby increasing the photoluminescence lifetime. In addition, a comparison of the trap density of states (Supplementary Fig. 20b) also indicates that Sr is a better dopant compared with Ca and Ba, consistent with the microstrain investigations discussed earlier. Thus, the following device studies focus on the CsFAGA:Sr composition.

To calculate the mobility (μ) after multisite doping, the space-charge-limited current method based on the hole-only device is performed (Supplementary Fig. 21). The CsFAGA:Sr crystal has an increased mobility of 288 cm^2 V^{-1} s^{-1}, compared with 241 and 162 cm^2 V^{-1} s^{-1} of CsFAGA and CsFA, respectively. The photoconductivity measurement is often used to characterize the $\mu\tau$ product for detectors, and the surface recombination velocity s can also

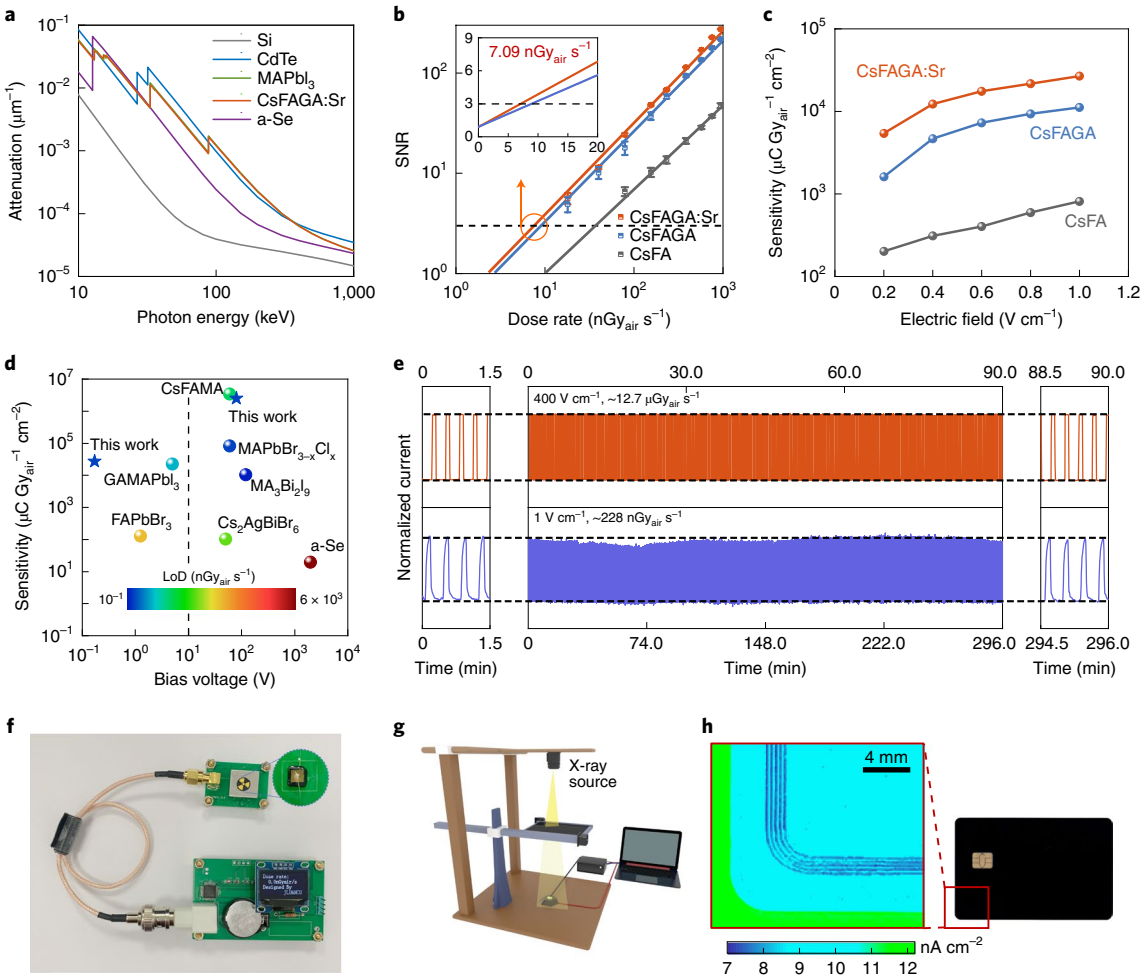

Fig. 4 | X-ray detection and imaging. a, Attenuation coefficient of different commercial semiconductors and perovskite single crystals. **b**, SNR dependent on the X-ray dose rate for the CsFA, CsFAGA and CsFAGA:Sr detectors, and the error bars are given according to variations in the current signal. The LoD of 7.09 nGy_{air} s^{-1} is derived from the fitting line with an SNR of 3. **c**, Sensitivity of X-ray detectors under different electric fields. **d**, Comparison of the sensitivity and LoD of representative X-ray detectors with different operating voltages: a-Se (ref. [5]), CsFAMA (ref. [14]), $FAPbBr_3$ (ref. [55]), $MA_3Bi_2I_9$ (ref. [56]), $Cs_2AgBiBr_6$ (ref. [57]), $MAPbBr_{3-x}Cl_x$ (ref. [58]), $GAMAPbI_3$ (ref. [59]). **e**, Operational stability test of the CsFAGA:Sr detector. **f**, Prototype of a portable X-ray monitor, powered by a button cell with an electric field of 1 V cm^{-1} for X-ray detection. **g**, Schematic of the X-ray imaging system. **h**, X-ray image of a bank card.

be obtained by fitting the photocurrent to the Hecht equation. The current–voltage (I–V) curve and fitting curve of the detector are shown in Fig. 3a. Compared with CsFA, the CsFAGA:Sr sample shows an enhanced $\mu\tau$ product of 1.29×10^{-2} cm^2 V^{-1} and decreased s of 82 cm s^{-1}.

We then investigate the detector performance. In Fig. 3b, the CsFAGA:Sr detector shows the lowest dark-current density of 1.0×10^{-9} A cm^{-2} at −1.0 V bias compared with other detectors, which is consistent with the conductivity calculated by the space-charge-limited current method ($\sigma_{CsFAGA:Sr}<\sigma_{CsFAGA}<\sigma_{CsFA}$). The CsFAGA:Sr detector has the lowest noise (4×10^{-14} A $Hz^{-1/2}$) (Supplementary Fig. 22). The external quantum efficiency of the CsFAGA:Sr detector at 800 nm increases from 15% of the value of CsFA to 18%, corresponding to a responsivity (R) of 0.12 A W^{-1} (Supplementary Figs. 23 and 24). The specific detectivity (D^*) of the CsFAGA:Sr detector determined by the noise current and responsivity (Fig. 3c) is close to 6×10^{11} Jones at 800 nm. As shown in Fig. 3d, the 3 dB cutoff frequency for the CsFAGA:Sr detector is 880 Hz, which is much faster than that of CsFAGA (720 Hz) and CsFA (478 Hz) detectors. Finally, the response stability of the devices is systematically studied and the results are shown in Fig. 3e. After a continuous test for 180 days, CsFAGA:Sr detectors maintain a stable response with less than 10% decay. In addition, given its high-temperature stability, the CsFAGA:Sr detector can work continuously for over 30 min at 125 °C. The long-term operational stability and thermal resistance ensure the long-term performance to meet specific standards[48].

The excellent photodetection performance indicates the potential applications of our perovskite single crystals for X-ray detection. As shown in Fig. 4a, simulation calculations (obtained from the NIST database[49]) show that the CsFAGA:Sr crystal has a similar α value as $MAPbI_3$ and CdTe, which is much higher than that of Si. By testing the relationship between current density and dose rate under 27 and 60 kVp X-rays (Supplementary Fig. 25), the response of the CsFAGA:Sr detector at the same dose rate is around 40 times higher than that of the CsFA detector. According to the definition of the International Union of Pure and Applied Chemistry, LoD corresponds to the dose rate when the generated signal is greater than three times the noise level[50]. As shown in Fig. 4b, by fitting the SNR at different doses, the obtained LoD is as low as 7.09 nGy_{air} s^{-1} when SNR = 3, which shows a significant decrease compared with both CsFAGA and CsFA devices. A low LoD of 7.09 nGy_{air} s^{-1} is among the best results of perovskite X-ray detectors until now (Supplementary Table 6).

In addition to the LoD, sensitivity is also an important parameter for evaluating the overall performance of the detector. The CsFAGA:Sr detector reaches a sensitivity of $(2.5 \pm 0.2) \times 10^6$ μC Gy_{air}^{-1} cm^{-2} under an electric field of 400 V cm^{-1} for 60 kVp X-rays (Supplementary Fig. 26a). In addition, the dark-current drift of CsFAGA:Sr under a high electric field is beyond one order of magnitude lower than that of CsFA (Supplementary Fig. 27), suggesting the effective suppression of ion migration[10]. Normally, a high bias field can lead to better charge collection and increased sensitivity. However, it raises concerns about system complexity for mobile equipment. Therefore, we also characterize the performance of X-ray detectors under low electric fields. Encouragingly, the CsFAGA:Sr device operated under a field of 1 V cm^{-1} still exhibits a high sensitivity of up to 2.7×10^4 μC Gy_{air}^{-1} cm^{-2} (Fig. 4c), which is about 2 and 33 times higher than that of CsFAGA and CsFA devices, respectively, at a dose rate of 155 nGy_{air} s^{-1}. Moreover, we achieve a stable sensitivity ($(2.6 \pm 0.1) \times 10^4$ μC Gy_{air}^{-1} cm^{-2}) of the CsFAGA:Sr device characterized under different dose rates (18–940 nGy_{air} s^{-1}) (Supplementary Fig. 26). The excellent performance is comparable to those of state-of-the-art perovskite detectors measured under much higher voltages (Fig. 4d and Supplementary Table 6). We notice that the drift length of the photocarriers under such a low electric field is smaller than the perovskite thickness; the underlying mechanism requires further investigations.

Another critical parameter that is important for future applications is long-term stability. As shown in Fig. 4e, the CsFAGA:Sr detector exhibits excellent stability with no attenuation under long-term continuous operation at 1 and 400 V cm^{-1}. Furthermore, after storage of 180 days, CsFAGA:Sr detectors without encapsulation retain excellent X-ray performance with a reduction in signal current within 10% (Supplementary Fig. 28).

The excellent stability, coupled with the predominant LoD and high sensitivity of the CsFAGA:Sr detector achieved under a low field, make our CsFAGA:Sr detectors especially attractive for low-bias portable applications, such as mobile medical equipment[51] and hand-held environmental radiation monitors[52]. A prototype X-ray monitor with low energy consumption has been successfully developed to highlight its excellent performance (Fig. 4f, Supplementary Fig. 29 and Supplementary Video 1). Powered by a button cell, the low LoD in the range of nGy_{air} s^{-1} indicates a great breakthrough in the balance between performance and power consumption for portable X-ray equipment.

Another application enabled by the excellent features of our CsFAGA:Sr detector is high-quality X-ray imaging. As shown in Supplementary Fig. 30, the CsFAGA:Sr device has a faster X-ray response than that of CsFA and CsFAGA devices, which is crucial for scanning imaging. As shown in Fig. 4g, an *x*–*y* scanning imaging system is built, using which a high-quality image of the internal coil of the card is achieved (Fig. 4h)[53], with a width of about 1.5 mm. To evaluate the imaging resolution of the CsFAGA:Sr detector, a one-dimensional scan was performed on a mask with a 150 μm channel under the detection area of 100×200 $μm^2$. As illustrated in Supplementary Fig. 31, high-precision scanning imaging was realized by adjusting the integrated reading time of the signal current. The imaging resolution was calculated to be 8.0 lp mm^{-1} using the slanted-edge method[54], demonstrating its immense potential for future X-ray imaging applications at a low bias (Supplementary Fig. 32).

Conclusion

In summary, we demonstrate a synergistic strain engineering strategy to obtain high-quality perovskite single crystals with excellent stability, by incorporating foreign cations at both A and B sites to fine-tune the structural and optoelectronic properties. The incorporation of GA on the A site effectively suppresses halide vacancy formation, whereas B-site doping with alkaline-earth metal can relieve the microstrain induced by A-site alloying, where Sr dopants at low concentrations prove to be especially effective. As a result, the detector based on dual-site-doped perovskite single crystals reaches an excellent sensitivity of $(2.6 \pm 0.1) \times 10^4$ μC Gy_{air}^{-1} cm^{-2} under a low field of 1 V cm^{-1}, a state-of-the-art detectable dose rate of 7.09 nGy_{air} s^{-1} and long-term stability beyond half a year. We have developed a novel prototype X-ray monitor with a low LoD in the range of nGy_{air} s^{-1} powered by coin-cell batteries. Besides X-ray detection, we believe that the material design strategy developed in our work can provide new insights into the challenges towards γ-ray spectrum acquisition and other commercial perovskite optoelectronic applications.

Online content

Any methods, additional references, Nature Research reporting summaries, source data, extended data, supplementary information, acknowledgements, peer review information; details of author contributions and competing interests; and statements of data and code availability are available at https://doi.org/10.1038/s41566-022-01024-9.

Received: 23 September 2021; Accepted: 16 May 2022;
Published online: 18 July 2022

References

1. Min, H. et al. Perovskite solar cells with atomically coherent interlayers on SnO_2 electrodes. *Nature* **598**, 444–450 (2021).
2. Chen, Q. et al. All-inorganic perovskite nanocrystal scintillators. *Nature* **561**, 88–93 (2018).
3. Bao, C. et al. Bidirectional optical signal transmission between two identical devices using perovskite diodes. *Nat. Electron.* **3**, 156–164 (2020).
4. He, Y. et al. $CsPbBr_3$ perovskite detectors with 1.4% energy resolution for high-energy γ-rays. *Nat. Photon.* **15**, 36–42 (2021).
5. Kasap, S. O. X-ray sensitivity of photoconductors: application to stabilized a-Se. *J. Phys. D* **33**, 2853 (2000).
6. Zhao, W. et al. Digital radiology using active matrix readout of amorphous selenium: detectors with high voltage protection. *Med. Phys.* **25**, 539–549 (1998).
7. Beutel, J., Kundel, H. L. & Metter, R. L. *Handbook of Medical Imaging: Physics and Psychophysics* (SPIE Press, 2000).
8. Szeles, C. CdZnTe and CdTe materials for X-ray and gamma ray radiation detector applications. *Phys. Stat. Sol. B* **241**, 783–790 (2004).
9. He, Y., Hadar, I. & Kanatzidis, M. G. Detecting ionizing radiation using halide perovskite semiconductors processed through solution and alternative methods. *Nat. Photon.* **16**, 14–26 (2022).
10. Liu, Y. et al. Ligand assisted growth of perovskite single crystals with low defect density. *Nat. Commun.* **12**, 1686 (2021).
11. Zhao, J. et al. Perovskite-filled membranes for flexible and large-area direct-conversion X-ray detector arrays. *Nat. Photon.* **14**, 612–617 (2020).
12. Kim, Y. et al. Printable organometallic perovskite enables large-area, low-dose X-ray imaging. *Nature* **550**, 87–91 (2017).
13. Deumel, S. et al. High-sensitivity high-resolution X-ray imaging with soft-sintered metal halide perovskites. *Nat. Electron.* **4**, 681–688 (2021).
14. Liu, Y. et al. Triple-cation and mixed-halide perovskite single crystal for high-performance X-ray imaging. *Adv. Mater.* **33**, 2006010 (2021).
15. Conings, B. et al. Intrinsic thermal instability of methylammonium lead trihalide perovskite. *Adv. Energy Mater.* **5**, 1500477 (2015).
16. van Breemen, A. J. J. M. et al. A thin and flexible scanner for fingerprints and documents based on metal halide perovskites. *Nat. Electron.* **4**, 818–826 (2021).
17. Li, Z. et al. Stabilizing perovskite structures by tuning tolerance factor: formation of formamidinium and cesium lead iodide solid-state alloys. *Chem. Mater.* **28**, 284–292 (2016).
18. McMeekin, D. P. et al. A mixed-cation lead mixed-halide perovskite absorber for tandem solar cells. *Science* **351**, 151–155 (2016).
19. Rehman, W. et al. Photovoltaic mixed-cation lead mixed-halide perovskites: links between crystallinity, photo-stability and electronic properties. *Energy Environ. Sci.* **10**, 361–369 (2017).
20. Turren-Cruz, S. H., Hagfeldt, A. & Saliba, M. Methylammonium-free, high-performance, and stable perovskite solar cells on a planar architecture. *Science* **362**, 449–453 (2018).
21. Nazarenko, O. et al. Single crystals of caesium formamidinium lead halide perovskites: solution growth and gamma dosimetry. *NPG Asia Mater.* **9**, e373 (2017).

22. Wang, H. et al. Controllable $Cs_xFA_{1-x}PbI_3$ single-crystal morphology via rationally regulating the diffusion and collision of micelles toward high-performance photon detectors. *ACS Appl. Mater. Inter.* **11**, 13812–13821 (2019).
23. McMeekin, D. P. et al. Crystallization kinetics and morphology control of formamidinium–cesium mixed-cation lead mixed-halide perovskite via tunability of the colloidal precursor solution. *Adv. Mater.* **29**, 1607039 (2017).
24. Saidaminov, M. I. et al. Multi-cation perovskites prevent carrier reflection from grain surfaces. *Nat. Mater.* **19**, 412–418 (2020).
25. Saidaminov, M. I. et al. Suppression of atomic vacancies via incorporation of isovalent small ions to increase the stability of halide perovskite solar cells in ambient air. *Nat. Energy* **3**, 648–654 (2018).
26. Liu, Y. et al. Inch-sized high-quality perovskite single crystals by suppressing phase segregation for light-powered integrated circuits. *Sci. Adv.* **7**, eabc8844 (2021).
27. Yu, H. et al. Native defect-induced hysteresis behavior in organolead iodide perovskite solar cells. *Adv. Funct. Mater.* **26**, 1411–1419 (2016).
28. Swarnkar, A., Mir, W. J. & Nag, A. Can B-site doping or alloying improve thermal- and phase-stability of all-inorganic $CsPbX_3$ (X = Cl, Br, I) perovskites. *ACS Energy Lett.* **3**, 286–289 (2018).
29. Zhou, Y. et al. Metal-doped lead halide perovskites: synthesis, properties, and optoelectronic applications. *Chem. Mater.* **30**, 6589–6613 (2018).
30. Yang, Z. et al. Anchored ligands facilitate efficient B-site doping in metal halide perovskites. *J. Am. Chem. Soc.* **141**, 8296–8305 (2019).
31. Navas, J. et al. New insights into organic–inorganic hybrid perovskite $CH_3NH_3PbI_3$ nanoparticles. An experimental and theoretical study of doping in Pb^{2+} sites with Sn^{2+}, Sr^{2+}, Cd^{2+} and Ca^{2+}. *Nanoscale.* **7**, 6216–6229 (2015).
32. Hwang, H. Y. et al. Lattice effects on the magnetoresistance in doped $LaMnO_3$. *Phys. Rev. Lett.* **75**, 914 (1995).
33. Nayak, P. K. et al. Impact of Bi^{3+} heterovalent doping in organic–inorganic metal halide perovskite crystals. *J. Am. Chem. Soc.* **140**, 574–577 (2018).
34. Wang, J. T. W. et al. Efficient perovskite solar cells by metal ion doping. *Energy Environ. Sci.* **9**, 2892–2901 (2016).
35. Phung, N. et al. The doping mechanism of halide perovskite unveiled by alkaline earth metals. *J. Am. Chem. Soc.* **142**, 2364–2374 (2020).
36. Moloney, E. G., Yeddu, V. & Saidaminov, M. I. Strain engineering in halide perovskites. *ACS Mater. Lett.* **2**, 1495–1508 (2020).
37. Chen, L. et al. Toward long-term stability: single-crystal alloys of cesium-containing mixed cation and mixed halide perovskite. *J. Am. Chem. Soc.* **141**, 1665–1671 (2019).
38. Ko, B. & Jung, H. Crystal preferred orientation of an amphibole experimentally deformed by simple shear. *Nat. Commun.* **6**, 6586 (2015).
39. Pham, N. D. et al. Tailoring crystal structure of $FA_{0.83}Cs_{0.17}PbI_3$ perovskite through guanidinium doping for enhanced performance and tunable hysteresis of planar perovskite solar cells. *Adv. Funct. Mater.* **29**, 1806479 (2019).
40. Zhou, Y. et al. Enhanced incorporation of guanidinium in formamidinium-based perovskites for efficient and stable photovoltaics: the role of Cs and Br. *Adv. Funct. Mater.* **29**, 1905739 (2019).
41. Jodlowski, A. D. et al. Large guanidinium cation mixed with methylammonium in lead iodide perovskites for 19% efficient solar cells. *Nat. Energy* **2**, 972–979 (2017).
42. Nazarenko, O. et al. Luminescent and photoconductive layered lead halide perovskite compounds comprising mixtures of cesium and guanidinium cations. *Inorg. Chem.* **56**, 11552–11564 (2017).
43. Aschauer, U. et al. Strain-controlled oxygen vacancy formation and ordering in $CaMnO_3$. *Phys. Rev. B* **88**, 054111 (2013).
44. Zheng, X. et al. Improved phase stability of formamidinium lead triiodide perovskite by strain relaxation. *ACS Energy Lett.* **1**, 1014–1020 (2016).
45. Shannon, R. D. Revised effective ionic radii and systematic studies of interatomic distances in halides and chalcogenides. *Acta Crystallogr. A* **32**, 751–767 (1976).
46. Walsh, A. et al. Self-regulation mechanism for charged point defects in hybrid halide perovskites. *Angew. Chem.* **127**, 1811–1814 (2015).
47. Ming, W., Chen, S. & Du, M. H. Chemical instability leads to unusual chemical-potential-independent defect formation and diffusion in perovskite solar cell material $CH_3NH_3PbI_3$. *J. Mater. Chem. A* **4**, 16975–16981 (2016).
48. Dreike, P. L. et al. An overview of high-temperature electronic device technologies and potential applications. *IEEE Trans. Compon., Packag., Manuf. Technol. A* **17**, 594–609 (1994).
49. Berger, M. J. et al. *XCOM: Photon Cross Sections Database: NIST Standard Reference Database 8* (NIST, 2013); https://www.nist.gov/pml/xcom-photon-cross-sections-database
50. Thompson, M., Ellison, S. L. R. & Wood, R. Harmonized guidelines for single-laboratory validation of methods of analysis. *Pure Appl. Chem.* **74**, 835–855 (2002).
51. Thirimanne, H. M. et al. High sensitivity organic inorganic hybrid X-ray detectors with direct transduction and broadband response. *Nat. Commun.* **9**, 2926 (2018).
52. Yamamoto, S. & Hatazawa, J. Development of an alpha/beta/gamma detector for radiation monitoring. *Rev. Sci. Instrum.* **82**, 113503 (2011).
53. Wei, W. et al. Monolithic integration of hybrid perovskite single crystals with heterogenous substrate for highly sensitive X-ray imaging. *Nat. Photon.* **11**, 315–321 (2017).
54. Samei, E., Flynn, M. J. & Reimann, D. A. A method for measuring the presampled MTF of digital radiographic systems using an edge test device. *Med. Phys.* **25**, 102–113 (1998).
55. Yao, M. et al. High-temperature stable $FAPbBr_3$ single crystals for sensitive X-ray and visible light detection toward space. *Nano Lett.* **21**, 3947–3955 (2021).
56. Zheng, X. et al. Ultrasensitive and stable X-ray detection using zero-dimensional lead-free perovskites. *J. Energy Chem.* **49**, 299–306 (2020).
57. Pan, W. et al. $Cs_2AgBiBr_6$ single-crystal X-ray detectors with a low detection limit. *Nat. Photon.* **11**, 726–732 (2017).
58. Wei, H. et al. Dopant compensation in alloyed $CH_3NH_3PbBr_{3-x}Cl_x$ perovskite single crystals for gamma-ray spectroscopy. *Nat. Mater.* **16**, 826–833 (2017).
59. Huang, Y. et al. A-site cation engineering for highly efficient $MAPbI_3$ single-crystal X-ray detector. *Angew. Chem. Int. Ed.* **58**, 17834–17842 (2019).

Publisher's note Springer Nature remains neutral with regard to jurisdictional claims in published maps and institutional affiliations.

Open Access This article is licensed under a Creative Commons Attribution 4.0 International License, which permits use, sharing, adaptation, distribution and reproduction in any medium or format, as long as you give appropriate credit to the original author(s) and the source, provide a link to the Creative Commons license, and indicate if changes were made. The images or other third party material in this article are included in the article's Creative Commons license, unless indicated otherwise in a credit line to the material. If material is not included in the article's Creative Commons license and your intended use is not permitted by statutory regulation or exceeds the permitted use, you will need to obtain permission directly from the copyright holder. To view a copy of this license, visit http://creativecommons.org/licenses/by/4.0/.

© The Author(s) 2022

Methods

Crystal growth. All the series of MA-free perovskite single crystals were grown using the inverse temperature crystallization method[20,38]. Specifically, a stoichiometric molar ratio of CsFA precursor solution (1.0 M) was prepared by dissolving 619 mg FAI (3.6 mmol), 104 mg CsI (0.4 mmol), 220 mg $PbBr_2$ (0.6 mmol) and 1.54 g PbI_2 (3.4 mmol) compounds in 4 ml γ-butyralactone (GBL). On stirring for 12 h, all the clear solutions were filtered through a 0.2 μm polytetrafluoroethylene filter before being placed in a preheated (80 °C) oil bath. Then, the temperature was gradually increased at a rate of 2 K h^{-1} to 120 °C. Small crystals with sizes of 1–2 mm were collected. To obtain large-sized crystals, the method of seed crystal induction was adopted and the obtained small crystals with a regular shape were selected as seeds for another period of growth. Finally, 6–8 mm large-sized single crystals could be obtained. For $Cs_{0.1}FA_{0.9-z}GA_zPb(I_{0.9}Br_{0.1})_3$ ($z=0$, 0.03, 0.05, 0.08), a 1 M solution of GAI/FAI/CsI/PbI_2/$PbBr_2$ in GBL was prepared following a similar procedure, by dissolving the five compounds in a stoichiometric molar ratio. For alkaline-earth metals (Ca, Sr and Ba)-doped single crystal, a small amount of alkaline-earth metal iodides (CaI_2, SrI_2 and BaI_2) were dissolved into the solution of $Cs_{0.1}FA_{0.85}GA_{0.05}Pb(I_{0.9}Br_{0.1})_3$ at a specific concentration. The amounts of B-site dopants (0.25%, 0.50% and 1.00%) in the perovskite solution are calculated according to the molar ratio with Pb. Except the composition of the precursor solution, all the alloyed and doped crystals are fabricated under similar conditions.

Device fabrication. A semitransparent 25 nm gold anode was deposited on the top surface of the single crystal by thermal evaporation, generally using a mask to define the area of 0.3 × 0.3 cm^2. Then, an 80 nm gold cathode was deposited on the bottom surface or over 150 μm gallium cathode was contacted by coagulation for the X-ray detector and photodetector.

Assessment of electronic properties. The $\mu\tau$ product and s values were calculated according to the simplified single-carrier Hecht equation[60,61]: $I = \frac{I_0\mu\tau V}{L^2}\frac{1-\exp\left(-\frac{L^2}{\mu\tau V}\right)}{1+\frac{L}{V}\frac{s}{\mu}}$, where I_0 is the saturated photocurrent, L is the thickness of crystal and V is the applied bias. The SNR can be obtained by the following formula: $\mathrm{SNR} = \frac{I_{\mathrm{signal}}}{I_{\mathrm{noise}}} = \frac{J_p - J_d}{\sqrt{\frac{1}{N}\sum_i^N (J_i - J_p)^2}}$, where J_p is the average photocurrent density, J_d is the average dark-current density and J_i is the instantaneous value of the photocurrent.

Thermal and long-term stability measurements. To characterize the thermal stability, the signal response of the detector to a 450 nm LED (27 mW cm^{-2}) was recorded as the device was heated at 125 °C in a vacuum. During the experiment, only the detector attached to the target stage was heated using the hot plate, whereas the light source and test system were not intentionally heated. For the characterization of long-term stability, the signal response of the detector to a 450 nm LED (10 mW cm^{-2}) was collected under ambient conditions with 20–40% humidity.

X-ray detection measurement. All X-ray detection experiments were conducted on a home-made system housed in the chamber of a Rigaku Multiflex diffractometer. Device responses to X-rays were measured by a low-noise current preamplifier (SR570, Stanford Research Systems) under different bias voltages, which were applied by a function generator (DS345, Stanford Research Systems) and a Keithley 2400 sourcemeter. The fall time was calculated by subtracting the decay time of the signal current from 90% to 10%, that is, $T_{\mathrm{fall\ time}} = T_{10\%} - T_{90\%}$, under a dose rate of 232 nGy_{air} s^{-1}. The dose rate of the emerging X-ray was adjusted by changing the tube current and object positions, and the intensity was calibrated by an ion-chamber dose sensor (Radcal Accu-Gold+).

Data availability

The main data supporting the findings of this study are available within the Article and its Supplementary Information. Additional data are available from the corresponding authors upon reasonable request.

References

60. Androulakis, J. et al. Dimensional reduction: a design tool for new radiation detection materials. *Adv. Mater.* **23**, 4163–4167 (2011).
61. K Stoumpos, C. C. et al. Crystal growth of the perovskite semiconductor $CsPbBr_3$: a new material for high-energy radiation detection. *Cryst. Growth Des.* **13**, 2722–2727 (2013).

Acknowledgements

We thank Z. Wei, Y.-X. Xu, W. Zhang, M. Yao and H. Wang for helpful discussions. Funding: L.S. thanks National Natural Science Foundation of China (grant 61875072) and Key Research and Development Projects of Jilin Science and Technology Department (grant 20200401044GX). K.Y. thanks the financial support of the National Natural Science Foundation of China (grants 51863013 and 61874052) and Excellent Young Foundation of Jiangxi Province (grant 20192BCB23009). X.Z. thanks the National Natural Science Foundation of China (grant 62004182). F.G. thanks the Knut and Alice Wallenberg Foundation (Dnr KAW 2019.0082) and the Swedish Government Strategic Research Area in Materials Science on Functional Materials at Linköping University (faculty grant SFO-Mat-LiU no. 2009-00971).

Author contributions

K.Y. and L.S. conceived the idea and designed the experiments. K.Y., L.S. and F.G. supervised the project. M.X. and Z.P. prepared the samples and characterized their structural properties. K.F. conducted the DFT calculations. L.F. contributed to the XRD measurements of perovskite crystals. H.H. assisted with the simulations and discussions. F.G., C.B. and L.Z. contributed to the discussions and assisted in the research. J.J. systematically contributed to the X-ray detection, imaging and photoelectronic measurements. D.X. and X.Z. tested the X-ray detection performance of the detector. J.J., K.Y. and L.S. co-wrote the manuscript, and F.G. provided the revisions. All the authors discussed the results and commented on the manuscript.

Funding

Open access funding provided by Linköping University

Competing interests

The authors declare no competing interests.

Additional information

Supplementary information The online version contains supplementary material available at https://doi.org/10.1038/s41566-022-01024-9.

Correspondence and requests for materials should be addressed to Kai Yao, Liang Shen or Feng Gao.

Peer review information *Nature Photonics* thanks Igor Jovanovic and the other, anonymous, reviewer(s) for their contribution to the peer review of this work.

Reprints and permissions information is available at www.nature.com/reprints.